Journal of
Materials Chemistry A

ROYAL SOCIETY
OF CHEMISTRY

PAPER

View Article Online
View Journal | View Issue

Cite this: *J. Mater. Chem. A*, 2024, **12**, 20064

Short-range disorder mediated stability of Zn in rock-salt MgO beyond configurational entropy†

Shengnan Sun, ‡*[a] Jun Zhou, ‡[a] Shibo Xi,‡[b] Hui Ru Tan,[a] Fengxia Wei, [a] Debbie Hwee Leng Seng,[a] Wei Ying Lieu, [ac] Yi Ren,[a] Shijie Wang *[a] and Zhi Wei Seh *[a]

Received 1st April 2024
Accepted 3rd July 2024

DOI: 10.1039/d4ta02175d

rsc.li/materials-a

High-entropy rock-salt $Mg_{0.2}Co_{0.2}Ni_{0.2}Cu_{0.2}Zn_{0.2}O$ has been intensively studied in the energy field due to its unique composition–function relationship and synergistic effect. Entropy-stabilization of Cu and Zn in rock-salt $Mg_{0.2}Co_{0.2}Ni_{0.2}Cu_{0.2}Zn_{0.2}O$ is the key characteristic of this material. As a parent binary oxide, ZnO exists as wurtzite in nature. Herein, for the first time we investigated the role of late 3d transition metals Co, Ni and Cu in stabilizing Zn in MgO-based rock-salt oxides under the same configurational entropy condition and their structural stability in alkaline solutions. We found that Co, Ni and Cu can increase the Zn solubility in MgO-based rock-salt oxides, $Mg_{0.50}TM_{0.25}Zn_{0.25}O$ (TM = Co, Ni and Cu, configurational entropy 1.04 R), with Cu being the best. Simulation results show that the formation energy of Zn substitution for Mg is the lowest in $Mg_{0.50}Cu_{0.25}Zn_{0.25}O$. Moreover, Cu incorporation can create a wide metal–oxygen bond length distribution, which causes short-range disorder and enhances Zn stabilization. Surprisingly, CuO with square-planar Cu–O coordination is more effective in stabilizing rock-salt ZnO in MgO, compared to rock-salt CoO and NiO, as Cu^{2+} ions undergo splitting of e_g orbitals due to strong Jahn–Teller distortion. $Mg_{0.50}Cu_{0.25}Zn_{0.25}O$ with medium entropy 1.04 R can stabilize 25 at% Cu and 25 at% Zn simultaneously. Besides, the Ni substitution is found to be effective in improving the structural stability in alkaline solutions. This work gives insight into understanding the complementation of orbital distribution in high-entropy oxides for metal stabilization, and provides a rational composition design for applications in the energy field.

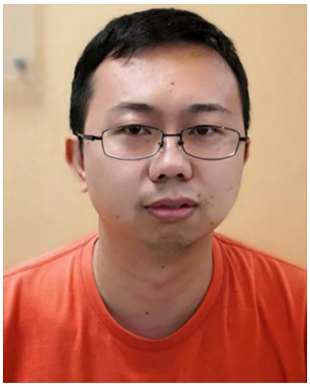

Shengnan Sun

Dr Shengnan Sun obtained his bachelor's and master's degrees in physics from Jilin University in 2010 and 2013, and PhD degree in materials from Nanyang Technological University in 2018. He worked in Nanyang Technological University (2017–2018), Weizmann Institute of Science (2018–2019) and Peking University (2019–2021). In 2021, he joined the Institute of Materials Research and Engineering, Agency for Science, Technology and Research and focused on battery and catalysis materials.

1. Introduction

High-entropy oxides (HEOs) are single-phase oxide solid solutions that have a configurational entropy greater than 1.5R and contain five or more cations.[1,2] Recently, HEOs with various crystal structures have demonstrated great potential and enhanced properties in the energy field,[3–5] such as in electrocatalysis and battery areas, due to the synergistic effect and unique composition–function relationship.[6,7] For example, enhanced oxygen evolution reaction (OER) on perovskite HEO $LaCr_{0.2}Mn_{0.2}Fe_{0.2}Co_{0.2}Ni_{0.2}O_{3-\delta}$ has been reported compared with all its parent compounds $LaMO_3$ (M = Cr, Mn, Fe, Co, Ni), which is ascribed to a synergistic effect in the adsorbate binding on several transition metal surfaces.[8] The HEO composition for better OER is also optimized by Nguyen *et al.* to $La(CrMnFeCo_2Ni)O_3$.[9] Enhanced OER is also observed on the

---

[a] *Institute of Materials Research and Engineering (IMRE), Agency for Science, Technology and Research (A*STAR), 2 Fusionopolis Way, Innovis #08-03, Singapore 138634, Republic of Singapore. E-mail: sun_shengnan@imre.a-star.edu.sg; sj-wang@imre.a-star.edu.sg; sehzw@imre.a-star.edu.sg*

[b] *Institute of Sustainability for Chemicals, Energy and Environment ($ISCE^2$), Agency for Science, Technology and Research (A*STAR), 1 Pesek Road, Jurong Island, Singapore 627833, Republic of Singapore*

[c] *Pillar of Engineering Product Development, Singapore University of Technology and Design, 8 Somapah Road, Singapore 487372, Republic of Singapore*

† Electronic supplementary information (ESI) available. See DOI: https://doi.org/10.1039/d4ta02175d

‡ S. S., J. Z. and S. X. contributed equally to this work.

spinel HEO $(Fe_{0.20}Co_{0.20}Ni_{0.20}Cu_{0.20}Zn_{0.20})Al_2O_4$ by Katzbaer *et al.*, which is attributed to a narrower band gap of the HEO than that of all parent spinel oxides.[10] We recently also found surface entropy evolution on spinel HEO $Zn(CrMnFeCoNi)_2O_4$ during OER cycling, accompanied by the changed reaction mechanism and promoted OER performance.[11] In the battery area, Liu *et al.* investigated the Co concentration effect in spinel $(CrFeMnNiCo_x)_3O_4$ on Li storage and found that higher Co concentrations contribute to higher Li storage capability.[12]

Besides perovskite and spinel HEOs, the rock-salt HEOs also exhibit excellent performance in catalysis,[13] anodes[14,15] and cathodes[16] in batteries, in particular, $Mg_{0.2}Co_{0.2}Ni_{0.2}Cu_{0.2}Zn_{0.2}O$, as a single phase stabilizing tenorite CuO and wurtzite ZnO in a single rock-salt structure by configurational entropy.[2] In the study by Liu *et al.*, $Mg_{0.2}Co_{0.2}Ni_{0.2}Cu_{0.2}Zn_{0.2}O$ has regulated electronic and geometric structures for superior intrinsic OER activity compared with CoO, NiO, and $Co_{0.5}Ni_{0.5}O$.[17] In our recent study, we found that the ammonia generation from nitrate reduction can be promoted on $Mg_{0.2}Co_{0.2}Ni_{0.2}Cu_{0.2}Zn_{0.2}O$ due to the spin-related Cu–Co pair.[13] In battery anodes, the cycling performance of $Mg_{0.2}Co_{0.2}Ni_{0.2}Cu_{0.2}Zn_{0.2}O$ and the synergy of cations have been intensively investigated. Sarkar *et al.* reported that entropy-stabilization in $Mg_{0.2}Co_{0.2}Ni_{0.2}Cu_{0.2}Zn_{0.2}O$ is beneficial to the Li-ion anode cycling stability, and the removal of any one of Co, Cu and Zn led to severe capacity degradation, especially Co.[14] Inactive material MgO and well-mixed cations in HEO are found to be essential to remarkable cycling, rate performance and high capacity by Qiu *et al.*[18] The lithiation–delithiation process of $Mg_{0.2}Co_{0.2}Ni_{0.2}Cu_{0.2}Zn_{0.2}O$ was investigated by Ghigna *et al.* using X-ray absorption spectroscopy (XAS) and they found that the reduction of cations begins from Cu to Co and Ni, followed by alloying Mg and Zn with Li, and furthermore the reaction is not fully reversible. They also suggest that both ZnO and MgO, especially MgO, are responsible for the high capacity compared with the oxides without Mg and Zn.[19] Moreover, in the XAS study by Wang *et al.*, metallic Co, Ni, Cu and Zn were observed and the rock-salt fcc Mg-dominated oxide matrix was left after lithiation, while Cu, Ni and a large fraction of Co were not being oxidized after delithiation.[20] Additionally, an improvement in Li-storage was reported in Li-substituted (MgCoNiZn)O[21] and (MgCoNiCuZn)O,[22] which is ascribed to the generation of oxygen vacancies. These findings imply the significance of the intrinsic composition–function relationship in cubic rock-salt oxides in electrocatalysis and Li-ion batteries.

While $Mg_{0.2}Co_{0.2}Ni_{0.2}Cu_{0.2}Zn_{0.2}O$ is considered as an entropy-stabilized oxide that stabilizes tenorite CuO and wurtzite ZnO in a single rock-salt structure, an investigation by Fracchia *et al.* demonstrates an important role of solubility in stabilizing Cu^{2+} ($t_{2g}{}^6e_g{}^3$ in 3d orbitals) in rock-salt oxides beyond configurational entropy.[23] Aamlid *et al.* categorized HEOs based on two characteristics, configurational entropy and entropy stabilization, that is, conventional solid solutions have low configurational entropy and are not entropy-stabilized while HEOs exhibit either configurational entropy (>1.5R) and/or entropy stabilization.[24] Brahlek *et al.* indicated that "entropy-stabilized" as a subset of "high-entropy" does not necessarily restrict the equilibrium entropy stabilization at room temperature.[25] Chen *et al.* experimentally pointed out that the formation of entropy-stabilized oxide does not necessarily need the configurational entropy to reach 1.5R and the critical temperature is significant in the annealing process for obtaining a single-phase state, taking medium configurational entropy $(Mg_{1/3}Co_{1/3}Ni_{1/3})_{1-x}Zn_xO$ for example.[26] Besides CuO, ZnO is also stabilized in the cubic rock-salt phase $Mg_{0.2}Co_{0.2}Ni_{0.2}Cu_{0.2}Zn_{0.2}O$. Differing from Cu^{2+}, Zn^{2+} has fully occupied 3d orbitals that are symmetrical in all directions with an electron configuration of $[Ar]3d^{10}$. Wurtzite ZnO has a typical sp^3 covalent bonding and a substantial ionic character.[27] ZnO is identified as a selective electrocatalyst for water oxidation (to generate hydrogen peroxide[28] and oxygen[29]), oxygen reduction reaction,[30] and CO_2 reduction,[31,32] and also as a suitable coating material for carbon anodes[33] and $LiCoO_2$ cathodes[34] in Li-ion batteries.

Inspired by the phase stabilization studies above and the composition–function relationship in electrocatalysis and batteries, herein for the first time, we unveil the Zn stabilization in the MgO-based rock-salt $Mg_{0.75-x}TM_xZn_{0.25}O$ (TM = Co, Ni and Cu) in powder form by focusing on the impact of late 3d transition metals Co, Ni and Cu. We chose MgO as the matrix due to the stable orbital $1s^22s^22p^6$ and non-magnetic properties of Mg^{2+} ions and its wide application in the energy field, for example, as a promoter in oxygen electrochemistry[35,36] and alcohol electrooxidation,[37,38] and as a coating to improve the electrode stability and capacity retention in batteries.[39–42] We found that the substitution of Co, Ni and Cu for Mg can increase the Zn solubility, among which Cu is the most effective, which is contrary to the intuition that CoO and NiO could be more effective because of their rock-salt structure. We also found that the Ni substitution is effective to improve the resistance to alkaline solutions and structural stability. Our results provide a design guideline for increasing the doping amount with the assistance of another transition metal, potentially in tuning Zn fractions and structural stability in solid solutions. We also for the first time indicate that the medium-entropy $Mg_{0.50}Cu_{0.25}Zn_{0.25}O$ (1.04R) suffices for stabilizing 25 at% Cu and 25 at% Zn in the rock-salt structure simultaneously.

2. Experimental

2.1 Materials

The oxides were synthesized by the sol–gel method as our previous report.[13] All chemicals were purchased from Sigma-Aldrich, including magnesium nitrate hexahydrate, cobalt nitrate hexahydrate, nickel nitrate hexahydrate, copper nitrate hemi(pentahydrate), zinc nitrate hexahydrate, nitric acid and citric acid, and urea. The metal nitrates, citric acid, and urea were dissolved in de-ionized water with the feeding mole ratio of 1 : 2 : 2 with less nitric acid under stirring. The solution was kept at ~95 °C until the gel formed and then dried at 170 °C in an oven overnight. This was followed by annealing at 1000 °C for 6 h at a 5 °C min^{-1} ramping rate and cooling down naturally. The stability of these oxides in alkaline solutions was evaluated by soaking these oxides in 2 M KOH for four weeks at room temperature under constant stirring. The oxides were collected by centrifugation at 8000 rpm and then drying in an oven overnight. The procedure of centrifugation is as follows. First, the alkaline centrifugate was removed by centrifugation. Then, the remaining oxides were washed by centrifugation at least twice in deionised water until the centrifugate was neutral, followed by a single wash in ethanol. X-ray diffraction (XRD, Bruker D8 Advance using Cu-Kα radiation) was used to characterize the crystal structure. Rietveld refinement was conducted using TOPAS v5, using fundamental parameters and the full axial model. A scanning electron microscope (SEM, JEOL JSM7600F equipped with an Oxford Instruments X-Max 50 mm^2 detector) and transmission electron microscope (TEM, FEI Titan equipped with an EDAX detector) were used to obtain the morphology and energy-dispersive X-ray spectroscopy (EDX) mapping. SEM-EDX was used to obtain the atomic ratios of metal elements by at least three independent measurements. The extended X-ray absorption fine structure (EXAFS) and X-ray absorption near edge structure (XANES) were studied at the Singapore Synchrotron Light Source, XAFCA beamline. X-ray photoelectron spectroscopy (XPS) was carried out using a Thermo Fisher Scientific Theta Probe and the binding energy was calibrated from carbon contamination (C 1s peak 284.8 eV). The number of XPS scans was adjusted as needed to achieve a high resolution and signal-to-noise ratio, considering the possibly low ratio of some metal elements. The XPS of commercial MgO (Kanto Chemical), CoO (Alfa Aesar), NiO (Sigma-Aldrich), CuO (Sigma-Aldrich) and ZnO (Kanto Chemical) were used as the control and reference.

2.2 Calculation

The solid solution of oxides is effectively modeled using special quasirandom structures (SQSs) generated by the Alloy Theoretic Automatic Toolkit (ATAT).[43] These SQSs are designed to minimize pair correlation differences with the ideally random alloy within a radius greater than 7 Å. The size of the SQSs is consistently set to 64 atoms, corresponding to 2 × 2 × 2 supercells of the rock-salt oxides. To perform further density functional theory (DFT) simulations, the generated SQS structures serve as initial configurations and are inputted into the Vienna *ab initio* Simulation Package (VASP 5.4.4).[44,45] The Perdew–Burke–Ernzerhof (PBE) approximation is utilized for the exchange–correlation functional, and the frozen-core all-electron projector augmented wave (PAW) method is employed to describe the electron–ion interaction.[46] The cutoff energy for the plane wave expansion is set to 600 eV. For all simulations, a Monkhorst-pack 6 × 6 × 6 *k*-point grid is applied. Moreover, the generalized gradient approximation (GGA) with Hubbard U is used specifically for the d orbitals of Ni, Cu, and Co.[47,48] The Hubbard U parameters for Ni, Cu, and Co are determined based on suggested values from systematic investigations carried out using high-throughput simulations.[49] While the lattice vectors of the SQS structures are kept fixed, their scale factors are optimized during the simulations. The atoms within the structure are fully relaxed until both the energy and force converge to 10^{-5} eV and 0.01 eV Å^{-1}, respectively.

3. Results & discussion

3.1 Material structure and morphology

Fig. 1a shows the XRD patterns of $Mg_{0.75}Zn_{0.25}O$, $Mg_{0.50}Co_{0.25}Zn_{0.25}O$, $Mg_{0.50}Ni_{0.25}Zn_{0.25}O$ and $Mg_{0.50}Cu_{0.25}Zn_{0.25}O$, and the Rietveld refinements can be found in Fig. S1–S4.† $Mg_{0.75}Zn_{0.25}O$ has an obvious rock-salt structure ($Fm\bar{3}m$, lattice parameter a = 4.2278 Å) and contains the second phase wurtzite ZnO (1.52 wt%). The diffraction peaks corresponding to the rock-salt structure shift to a lower angle compared to the standard rock-salt MgO, indicating that Zn introduction increases the lattice constant according to Bragg's law. Such an increase in the lattice constant is consistent with the effective ionic radii order: Zn^{2+} (0.745 Å) > Mg^{2+} (0.720 Å).[50] When substituting Co, Ni and Cu for Mg, the wurtzite ZnO peaks became weaker and even disappeared. $Mg_{0.50}Co_{0.25}Zn_{0.25}O$ is a single rock-salt phase (lattice parameter a = 4.2428 Å) without the wurtzite ZnO impurity, which indicates that Co is effective in increasing Zn solubility in rock-salt MgO. However, the diffraction peaks of $Mg_{0.50}Co_{0.25}Zn_{0.25}O$ have lower intensities compared with that of $Mg_{0.75}Zn_{0.25}O$, indicating that Co substitution reduces the crystallization. The Ni substitution for Mg only increases Zn solubility and rock-salt structure crystallization (lattice parameter a = 4.2200 Å), however an impurity-free single rock-salt $Mg_{0.50}Ni_{0.25}Zn_{0.25}O$ could not be obtained (0.088 wt% ZnO). Apart from Co and Ni substitution, substituting Cu for Mg also increases Zn solubility in rock-salt MgO and makes $Mg_{0.50}Cu_{0.25}Zn_{0.25}O$ a single rock-salt phase (lattice parameter a = 4.2394 Å). Different from the XRD profiles of $Mg_{0.50}Co_{0.25}Zn_{0.25}O$ and $Mg_{0.50}Ni_{0.25}Zn_{0.25}O$, $Mg_{0.50}Cu_{0.25}Zn_{0.25}O$ has a strong (111) diffraction peak, indicating that Cu can increase the order in the [111] direction. It is well known that the (111) planes in rock-salt oxides consist of either metal atoms or oxygen atoms exclusively, and metal atoms contribute more than oxygen atoms in the diffraction peak intensity due to their relatively higher masses. $Mg_{0.50}Cu_{0.25}Zn_{0.25}O$ has a low intensity ratio of $I(200)/I(111)$, indicative of the less ordered (200) planes, which can be explained using the Jahn–Teller effect induced by Cu^{2+}.[51] To further compare the enhancement effect between Co and Cu on Zn solubility, we increased the Zn fraction to 30 at% and found that Cu is more effective than Co (Fig. S5†).

The SEM images show that $Mg_{0.50}TM_{0.25}Zn_{0.25}O$ (TM = Co, Ni and Cu) exist in the form of particles without regular morphology (Fig. 1b and S6†). The particles have good crystallization. For example, the TEM images show the (111), (200) and (220) lattices of $Mg_{0.50}Cu_{0.25}Zn_{0.25}O$, corresponding to 0.243 nm, 0.210 nm and 0.151 nm, respectively, consistent with the XRD pattern (Fig. 1c and S7†). The selected area electron diffraction (SAED) pattern (Fig. 1d) shows that the particles exist in the form of single crystals, corresponding to the location in Fig. 1c. The SEM-EDX mapping results indicate that the element distribution is homogeneous in these three oxides (Fig. S8†). Furthermore, the metal element ratios in the oxides are close to the metal precursor feeding ratios (Tables S3–S5†). Within a single particle, the element distribution is also homogeneous as evidenced by the TEM-EDX mapping of Mg, Cu, Zn and O in Fig. 1e.

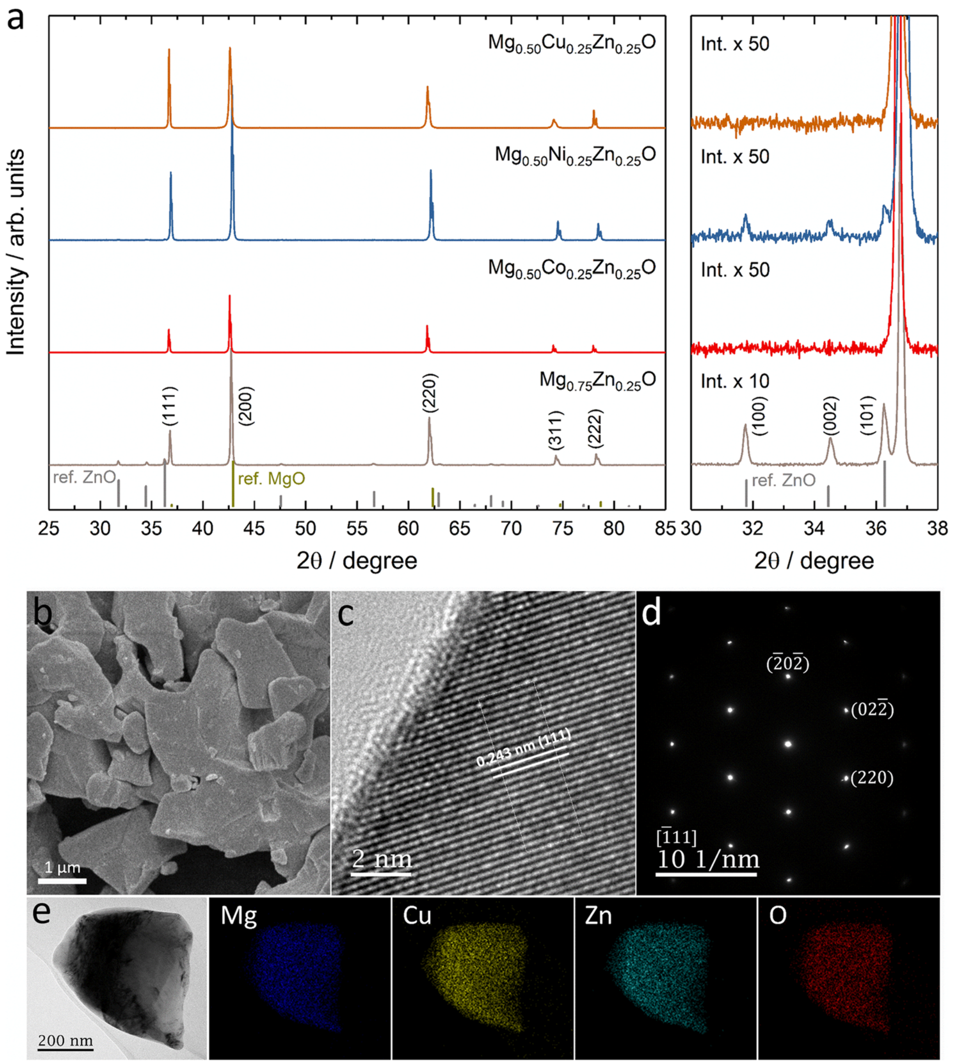

Fig. 1 (a) XRD patterns of Co, Ni and Cu substituted $Mg_{0.75}Zn_{0.25}O$. XRD standard peak: MgO refers to PDF 00-045-0946 and ZnO refers to PDF 00-036-1451. (b) SEM image, (c) HRTEM image, (d) SAED pattern at the location in (c), and (e) TEM-mapping of $Mg_{0.50}Cu_{0.25}Zn_{0.25}O$.

Fig. 2 shows the k^3-weighting Fourier-transformed EXAFS (FT-EXAFS) results of Zn, Co, Ni and Cu in $Mg_{0.50}Co_{0.25}Zn_{0.25}O$, $Mg_{0.50}Ni_{0.25}Zn_{0.25}O$ and $Mg_{0.50}Cu_{0.25}Zn_{0.25}O$. The experimental EXAFS data can be found in Fig. S9 and S10.† In Fig. 2a, the peaks at around 1.66–1.69 Å and at 2.58 Å are attributed to the first-shell neighbour (Zn–O) and the second-shell neighbour Zn–metal scattering, respectively. Similar attributions can made to Co/Ni/Zn for the peaks in Fig. 2b.[52] Considering that the peak position at distances in FT-EXAFS is shifted from the real interatomic distance by 0.2–0.5 Å,[53] the EXAFS fitting is performed to obtain the nearest metal–oxygen and metal–metal distances as well as the coordination number. The fitted results for the first and second shells and the parameters can be found in Fig. 2, S11, Tables 1 and S1.† Theoretically, in ideal cubic rock-salt oxides the first-shell coordination number of metal with oxygen is 6 and the second-shell coordination number of metal with metal is 12. From Table 1, in $Mg_{0.50}Co_{0.25}Zn_{0.25}O$ and $Mg_{0.50}Ni_{0.25}Zn_{0.25}O$, the first-shell distances of Zn–O, Co–O, and Ni–O are close (~2.12 Å). The first-shell coordination number of Zn with O is around 5.7, which is lower than that of Co/Ni (around 6.3). The first-shell Zn–O distance and the coordination number of Zn in $Mg_{0.50}Cu_{0.25}Zn_{0.25}O$ are close to that in $Mg_{0.50}Co_{0.25}Zn_{0.25}O$ and $Mg_{0.50}Ni_{0.25}Zn_{0.25}O$, while the Cu–O distance (2.00 Å) and coordination number (3.1) are much smaller compared with Zn, Co and Ni. It could be caused by the Jahn–Teller distortion of Cu^{2+} ions.[51] In $Mg_{0.50}Cu_{0.25}Zn_{0.25}O$, the second-shell Zn–Mg/Cu/Zn distances are in the range of 2.98 to 3.00 Å. The coordination number of Zn with Mg is 7.9, which is larger than 6 (based on the metal stoichiometric ratio in the oxides), while the coordination number of Zn with Cu/Zn is 2.1, smaller than 6. This suggests that more Mg instead of Cu/Zn occupies the second shell of Zn. Cu has a normal coordination number of 6.1 with Mg and a smaller one of 1.2 with Cu/Zn, which means Cu has a low coordination environment in the second shells, suggesting the less ordered structure around Cu. In $Mg_{0.50}Ni_{0.25}Zn_{0.25}O$, the same Zn–Mg and Ni–Mg distance 2.96 Å is calculated in the second shell of Zn and Ni with the coordination numbers 7.9 and 8.1, respectively. Zn–Ni/Zn and

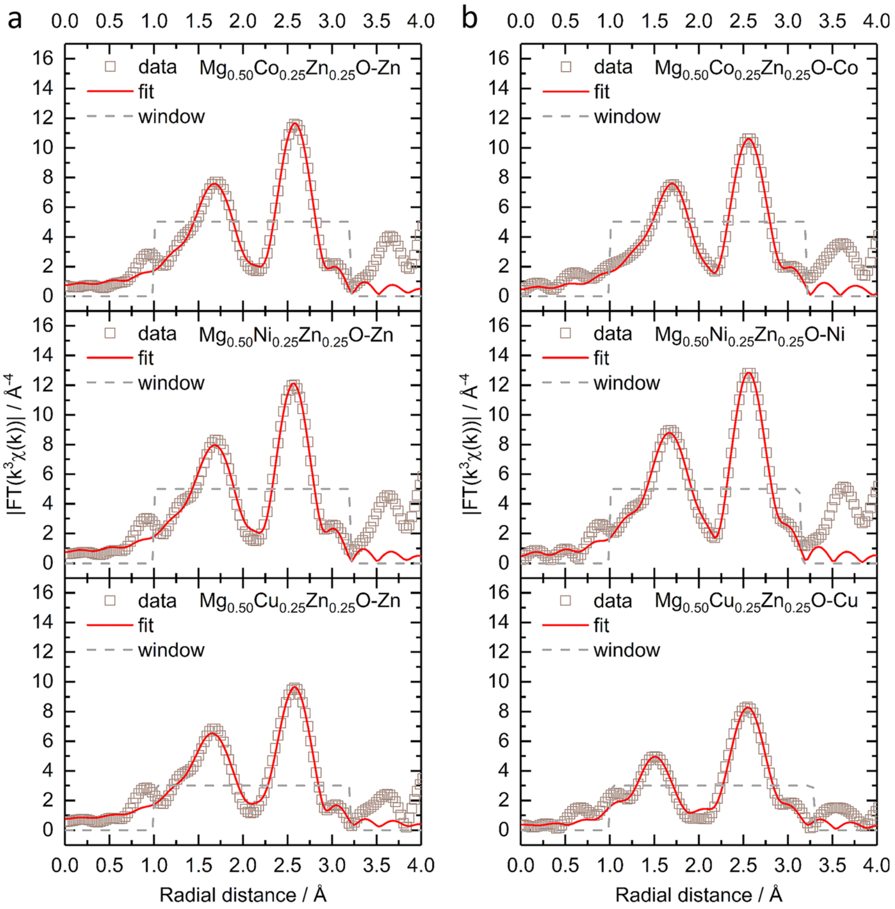

Fig. 2 The k^3-weighting FT-EXAFS and the fitting of (a) the Zn K-edge and (b) Co, Ni and Cu K-edges of $Mg_{0.50}TM_{0.25}Zn_{0.25}O$ (TM = Co, Ni, Cu) under a Hanning-shaped window.

Ni–Ni/Zn have close distances 2.98 Å and 2.97 Å, and coordination numbers 2.0 and 2.3 with Ni/Zn, respectively. Compared with $Mg_{0.50}Ni_{0.25}Zn_{0.25}O$ and $Mg_{0.50}Cu_{0.25}Zn_{0.25}O$, Zn in $Mg_{0.50}Co_{0.25}Zn_{0.25}O$ has a close coordination number (8.1) with Mg and a much smaller coordination number (0.2) with Co/Zn, suggesting Zn is less coordinated in the second shell, particularly with Co/Zn. In contrast to Zn, Co has a larger coordination number of 9.6 with Mg and 2.8 with Co/Zn. This indicates that more metals are around Co and less around Zn. Besides, Zn–Mg, Zn–Co/Zn, Co–Mg and Co–Co/Zn in $Mg_{0.50}Co_{0.25}Zn_{0.25}O$ have a very close distance around 2.98 Å.

Considering the deviation of the coordination number from ideal values, additional fitting has been performed by fixing the coordination numbers. For Co, Ni and Zn, the first-shell coordination number of the metal with oxygen is fixed to 6, while for Cu, 4 planar and 2 axial coordinating oxygens are considered.[54] Because the coordinating metals are randomly distributed and cannot be identified precisely,[55] the total second-shell coordination number of metal with metal is fixed to 12. The fitted results and the parameters applied can be found in Fig. S12, S13, Tables 2 and S2.† The fitted Zn–O distances are about 2.14 Å in $Mg_{0.50}Co_{0.25}Zn_{0.25}O$, $Mg_{0.50}Ni_{0.25}Zn_{0.25}O$ and $Mg_{0.50}Cu_{0.25}Zn_{0.25}O$, which are very close to the fitted values in Table 1. The Co–O and Ni–O distances remain unchanged for the two fittings. For Cu–O, the planar distance is 2.02 Å and the axial distance is 2.28 Å, which are close to reported values in $Mg_{0.2}Co_{0.2}Ni_{0.2}Cu_{0.2}Zn_{0.2}O$.[54–56] For $Mg_{0.50}Co_{0.25}Zn_{0.25}O$ and $Mg_{0.50}Ni_{0.25}Zn_{0.25}O$, the fitted second-shell

Table 1 EXAFS fitting results for interatomic distances and coordination numbers. For each element pair, the number before the slash is the distance between them, and the one after the slash is the coordination number of the first element with the second element

	Zn–O	TM–O	Zn–Mg	Zn–TM/Zn	TM–Mg	TM–TM/Zn
$Mg_{0.50}Co_{0.25}Zn_{0.25}O$	2.13 Å/5.6	2.12 Å/6.4	2.99 Å/8.1	2.99 Å/0.2	2.98 Å/9.6	2.98 Å/2.8
$Mg_{0.50}Ni_{0.25}Zn_{0.25}O$	2.12 Å/5.7	2.10 Å/6.2	2.96 Å/7.9	2.98 Å/2.0	2.96 Å/8.1	2.97 Å/2.3
$Mg_{0.50}Cu_{0.25}Zn_{0.25}O$	2.12 Å/5.7	2.00 Å/3.1	2.98 Å/7.9	3.00 Å/2.1	2.97 Å/6.1	2.99 Å/1.2

Table 2 EXAFS fitting results for interatomic distances and coordination numbers, fixing the coordination number to 6 for the first shell and 12 for the second shell. For each element pair, the number before the slash is the distance between them, and the one after the slash is the coordination number of the first element with the second element

	Zn–O	TM–O	Zn–Mg	Zn–TM/Zn	TM–Mg	TM–TM/Zn
$Mg_{0.50}Co_{0.25}Zn_{0.25}O$	2.14 Å/6	2.12 Å/6	3.02 Å/11.5	3.01 Å/0.5	2.98 Å/9.4	2.98 Å/2.6
$Mg_{0.50}Ni_{0.25}Zn_{0.25}O$	2.13 Å/6	2.10 Å/6	2.97 Å/9.0	2.97 Å/3.0	2.97 Å/8.9	2.97 Å/3.1
$Mg_{0.50}Cu_{0.25}Zn_{0.25}O$	2.14 Å/6	2.02 Å/4 2.28 Å/2	2.88 Å/9.7	2.75 Å/2.3	2.97 Å/8.7	2.99 Å/3.3

metal–metal distances do not change significantly before and after fixing the coordination numbers. In $Mg_{0.50}Cu_{0.25}Zn_{0.25}O$, the fitted Cu–Mg and Cu–Cu/Zn distances are the same as the values in Table 1, while a dramatic metal–metal distance decrease is observed in Zn–Mg and Zn–Cu/Zn. Though the second-shell coordination numbers for the specific metals still deviate from the ideal coordination numbers after fixing the total coordination number, the trend remains similar to that shown in Table 1.

3.2. Electronic states

The electronic states of Co, Ni, Cu and Zn were further investigated by XANES (Fig. S14†). No obvious change can be observed in the Zn K-edge XANES profile amongst $Mg_{0.50}Co_{0.25}Zn_{0.25}O$, $Mg_{0.50}Ni_{0.25}Zn_{0.25}O$ and $Mg_{0.50}Cu_{0.25}Zn_{0.25}O$ (Fig. S14a†), while their Zn profiles differ from those of ZnO and the reported profile.[57] In ZnO (Fig. S14a†), one small shoulder E1 at ∼9663.5 eV, peaks E2 at ∼9669.3 eV and E3 at ∼9680.3 eV, and EXAFS oscillation E4 at ∼9714.9 eV are observed, consistent with the reported ZnO profile by Rodrigues *et al.*[57] Moreover, the E3 peaks for Zn in $Mg_{0.50}Co_{0.25}Zn_{0.25}O$, $Mg_{0.50}Ni_{0.25}Zn_{0.25}O$ and $Mg_{0.50}Cu_{0.25}Zn_{0.25}O$ are shifted by ∼5 eV to higher energy with respect to ZnO, which is also consistent with the report on wurtzite ZnO and cubic ZnO.[58] This can be explained by the difference in the Zn chemical environment in these three oxides and wurtzite ZnO. This is in contrast to the Co and Ni XANES profiles of $Mg_{0.50}Co_{0.25}Zn_{0.25}O$ and $Mg_{0.50}Ni_{0.25}Zn_{0.25}O$, which have no obvious changes and energy shifts compared to commercial CoO and NiO (Fig. S14b and c†), thus suggesting that the Co and Ni valence states are close to +2. Fig. S14d† shows that the Cu XANES profile is different from that of commercial CuO, which can be explained that the environment of Cu in $Mg_{0.50}Cu_{0.25}Zn_{0.25}O$ is different from that in tenorite CuO. Besides XANES, XPS are used to further reveal the surface electronic state of $Mg_{0.50}TM_{0.25}Zn_{0.25}O$ (TM = Co, Ni, Cu) (Fig. 3 and S15†). The XPS results of commercial MgO, CoO, NiO, CuO and ZnO are also provided in Fig. S16 and S17† as references. The Zn 2p profiles have no obvious change among $Mg_{0.50}TM_{0.25}Zn_{0.25}O$ (TM = Co, Ni, Cu) (Fig. 3a, c and e), and the binding energies of Zn $2p_{3/2}$ (∼1021.3 eV) and Zn $2p_{1/2}$ (∼1044.4 eV) and their difference (∼23.1 eV) are almost the same as that of the commercial ZnO (Fig. S16c†). This indicates a valence state of +2 for Zn. The Co $2p_{3/2}$ spectrum in $Mg_{0.50}Co_{0.25}Zn_{0.25}O$ is split into three peaks at 779.8 eV, 781.5 eV and 786.5 eV, respectively (Fig. 3b), which have a similar profile to that of the commercial CoO (Fig. S17a†) and the report by Biesinger *et al.*[59] The binding energies of 779.8 eV and 786.5 eV can be assigned to Co^{2+} and the satellite, respectively. The attribution to the binding energy of 781.2 eV is still under debate. Some studies assigned it to Co^{2+},[60,61] while others to Co^{3+}.[59,62] The early work by McIntyre and Cook indicated that the Co formal oxidation states are hardly differentiated from the binding energy.[63] The Ni $2p_{3/2}$ profile has a main peak at 854.9 eV and a satellite peak at 860.8 eV (Fig. 3d), which agrees with our reported one in $Mg_{0.2}Co_{0.2}Ni_{0.2}Cu_{0.2}Zn_{0.2}O$. The main peak has no obvious doublet structure at 853.5 eV (local screening) and 855.4 eV (nonlocal screening)[52,64] like commercial NiO (Fig. S17c†). The missing peak can be explained by the negligible nonlocal screening contribution from Ni as the next nearest neighbours as the diluted NiO in the MgO–ZnO matrix,[65] which is in agreement with the report by Altieri *et al.*[66] The attribution of the Cu $2p_{3/2}$ profile in Fig. 3f is similar to our previous report[13] and commercial CuO in Fig. S17e.† The main difference is the relative intensity of Cu^{+} (932.5 eV) on the surface. Besides, no obvious changes of Mg 1s profiles are observed in $Mg_{0.50}TM_{0.25}Zn_{0.25}O$ (TM = Co, Ni, Cu) (Fig. S15†) and commercial MgO (Fig. S16†), indicating the existence of Mg^{2+} in the oxides. The O 1s has three distinct peaks at 529.3 eV, 531.0 eV and 533.0 eV (Fig. S15†), take the O 1s profile of $Mg_{0.50}Co_{0.25}Zn_{0.25}O$ as an example, which are assigned to the lattice oxygen, oxygen vacancy and chemically adsorbed oxygen, respectively.[21,67] The recent work by Frankcombe and Liu[68] pointed out that the binding energy of 531 eV is ascribed to the water molecules strongly bound to the surface as distinct from more loosely bound water at 533 eV.

3.3. Cu promoted Zn stabilization

To further investigate the effect of Cu on Zn stabilization in MgO-based rock-salt oxides, we kept the Zn fraction at 30 at% and further tune the relative ratios of Mg and Cu. From the XRD patterns in Fig. 4, $Mg_{0.70}Zn_{0.30}O$ has a more obvious wurtzite ZnO phase than $Mg_{0.75}Zn_{0.25}O$ in Fig. 1a. This suggests that ZnO further evolves when the Zn fraction increases from 25% in the $Mg_{1-x}Zn_xO$ series. As the Cu fraction increases to 10% and 20%, the ZnO diffraction peaks become increasingly weaker, which means that Cu is effective in stabilizing Zn and inhibiting the ZnO evolution in the rock-salt oxide, even though the amount of phase formation agent Mg decreases and is replaced by Cu. Meanwhile, an increasing (111) peak intensity can be observed, which indicates that the introduction of Cu improves the order in the [111] direction. In addition, the (200) peak becomes weaker gradually, which is caused by the Jahn–Teller distortion

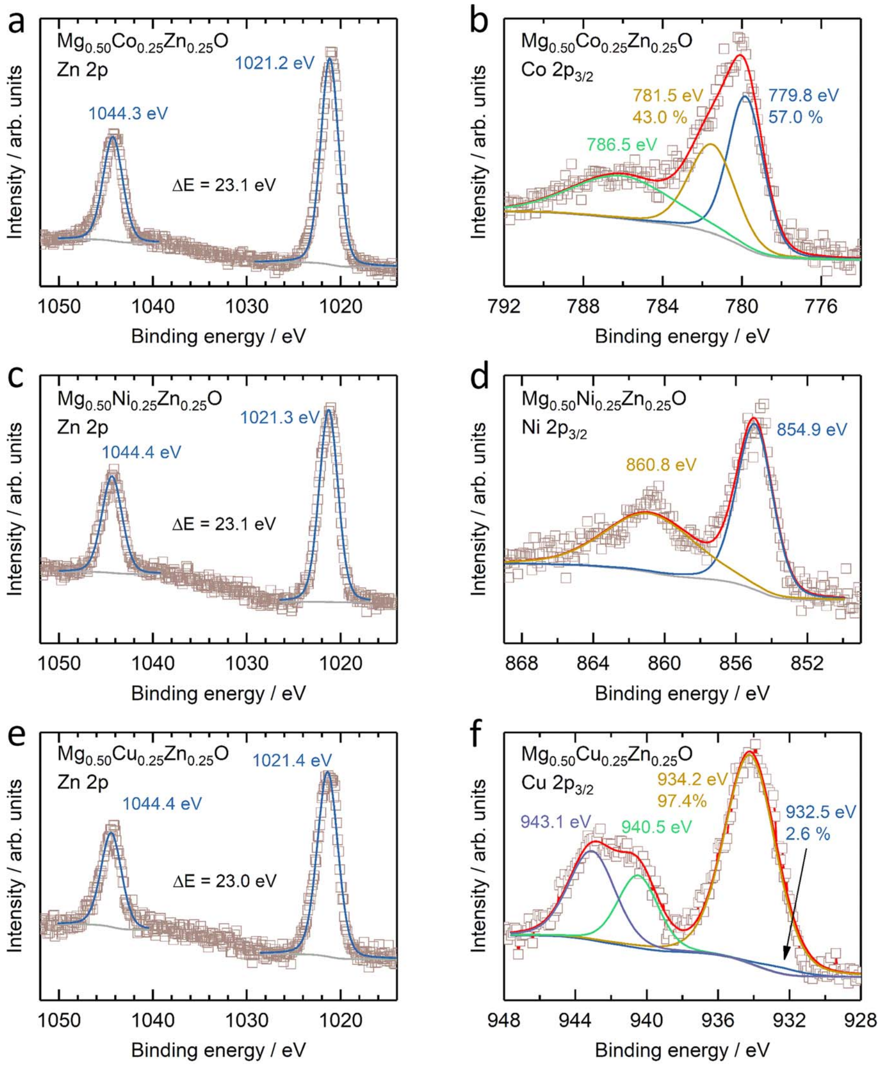

Fig. 3 XPS results of (a, c and e) Zn 2p and (b) Co $2p_{3/2}$, (d) Ni $2p_{3/2}$ and (f) Cu $2p_{3/2}$ of (a and b) $Mg_{0.50}Co_{0.25}Zn_{0.25}O$, (c and d) $Mg_{0.50}Ni_{0.25}Zn_{0.25}O$ and (e and f) $Mg_{0.50}Cu_{0.25}Zn_{0.25}O$.

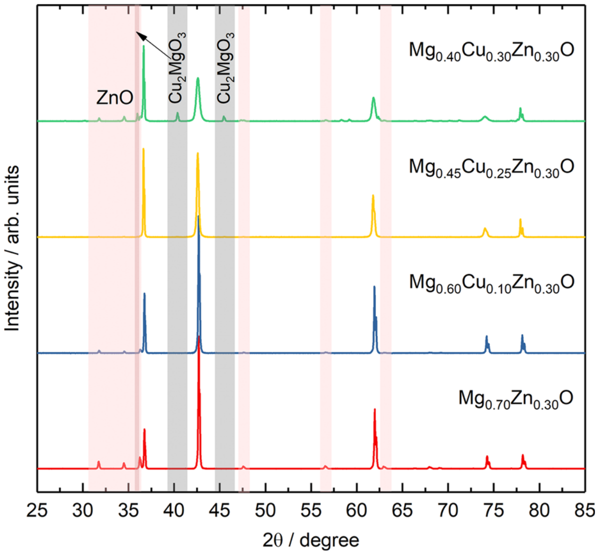

Fig. 4 XRD patterns of the $Mg_{0.70-x}Cu_xZn_{0.30}O$ series.

of Cu^{2+} ions.[51] The Rietveld refinements of $Mg_{0.70}Zn_{0.30}O$, $Mg_{0.60}Cu_{0.10}Zn_{0.30}O$ and $Mg_{0.45}Cu_{0.25}Zn_{0.30}O$ can be found in Fig. S18–S20.† There are no obvious attribution changes in the XPS profiles of $Mg_{0.45}Cu_{0.25}Zn_{0.30}O$ (Fig. S21†). When the Cu fraction reaches 30%, an obvious ZnO phase is observed again and a new Cu_2MgO_3 impurity appears. This means that the introduction of excess Cu does not contribute to Zn stabilization in the rock-salt oxide, and in contrast it causes Cu_2MgO_3 formation, which lowers Zn solubility in the rock-salt oxides.

3.4 Formation energy and bond length distribution

To gain deeper insights into the experimental findings, we further perform density functional theory (DFT) simulations for the three compositions: $Mg_{0.50}Co_{0.25}Zn_{0.25}O$, $Mg_{0.50}Ni_{0.25}Zn_{0.25}O$ and $Mg_{0.50}Cu_{0.25}Zn_{0.25}O$. Special quasirandom structures (SQSs) are used to model the solid solution state of these rock-salt oxides. As shown in Fig. 5a–c, the relaxed structures demonstrate significant differences. In the case of $Mg_{0.50}Cu_{0.25}Zn_{0.25}O$ (Fig. 5b), the inclusion of Cu atoms results in

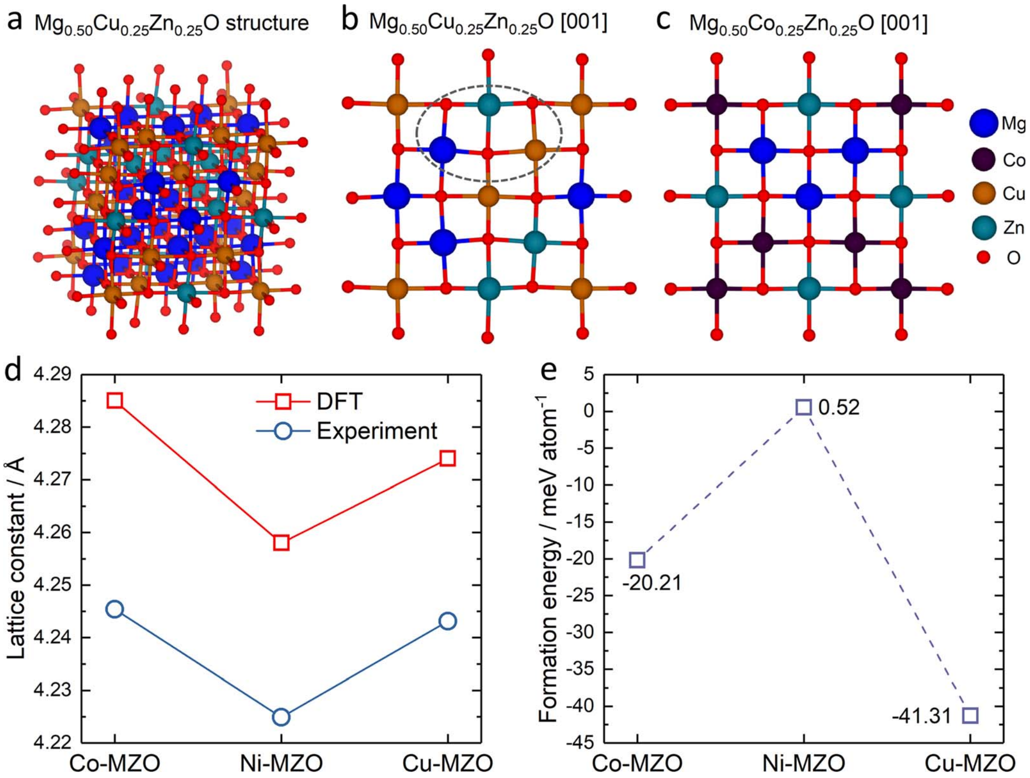

Fig. 5 The typical rock-salt structure generated from the high-entropy random model of (a) $Mg_{0.50}Cu_{0.25}Zn_{0.25}O$, the slice of (b) $Mg_{0.50}Cu_{0.25}Zn_{0.25}O$ and (c) $Mg_{0.50}Co_{0.25}Zn_{0.25}O$ viewed from the [001] direction; (d) the lattice constant from the relaxed structure and the experiment (XRD patterns), and (e) the average formation energy for substituting Mg by Zn in $Mg_{0.50}Co_{0.25}Zn_{0.25}O$ (Co–MZO), $Mg_{0.50}Ni_{0.25}Zn_{0.25}O$ (Ni–MZO) and $Mg_{0.50}Cu_{0.25}Zn_{0.25}O$ (Cu–MZO).

noticeable lattice distortions. This distortion can be attributed to the Jahn–Teller effect induced by Cu^{2+}. The observed deviation in the oxygen positions of the relaxed structure of $Mg_{0.50}Cu_{0.25}Zn_{0.25}O$ aligns with the low intensity of the metal–oxygen peak in the EXAFS results. Conversely, the lattice distortion is found to be less profound in $Mg_{0.50}Co_{0.25}Zn_{0.25}O$ and $Mg_{0.50}Ni_{0.25}Zn_{0.25}O$ (Fig. 5c and S22†). The trend of the lattice constants obtained from the relaxed models is also consistent with our experimental observations (Fig. 5d), further strengthening the reliability of our simulations.

To investigate the influence of lattice distortions on Zn solubility in MgO, we calculated the formation energies for the substitution of Mg by Zn in the three structures mentioned above. The reference structures to obtain the formation energies are constructed by replacing all the Zn atoms with Mg atoms for $Mg_{0.50}Co_{0.25}Zn_{0.25}O$, $Mg_{0.50}Ni_{0.25}Zn_{0.25}O$, $Mg_{0.50}Cu_{0.25}Zn_{0.25}O$ and $Mg_{0.75}Zn_{0.25}O$ while keeping the atom positions of the gnateater structures fixed. The calculated average formation energies for Zn substitution of Mg for $Mg_{0.50}Co_{0.25}Zn_{0.25}O$, $Mg_{0.50}Ni_{0.25}Zn_{0.25}O$ and $Mg_{0.50}Cu_{0.25}Zn_{0.25}O$, with respect to $Mg_{0.75}Zn_{0.25}O$, are −20.21 meV, 0.52 meV, and −41.31 meV, respectively (Fig. 5e). These results indicate that the inclusion of Cu or Co atoms stabilizes the solubility of Zn in MgO, while the presence of Ni has negligible effects. Furthermore, the lowest formation energy is observed for $Mg_{0.50}Cu_{0.25}Zn_{0.25}O$, suggesting that Zn is most readily stabilized in this composition among the three samples investigated. These findings are consistent with the XRD results obtained for $Mg_{0.50}Co_{0.25}Zn_{0.25}O$, $Mg_{0.50}Ni_{0.25}Zn_{0.25}O$ and $Mg_{0.50}Cu_{0.25}Zn_{0.25}O$.

Apart from the different formation energies, we can also observe the change in the metal–oxygen bond length distribution in the relaxed $Mg_{0.50}Co_{0.25}Zn_{0.25}O$, $Mg_{0.50}Ni_{0.25}Zn_{0.25}O$ and $Mg_{0.50}Cu_{0.25}Zn_{0.25}O$ structures (Fig. 6). In $Mg_{0.50}Co_{0.25}Zn_{0.25}O$, the Mg–O, Co–O and Zn–O bond lengths are distributed and concentrated in the ranges of 2.10–2.15 Å, 2.13–2.18 Å, and 2.13–2.18 Å, with their average bond lengths being 2.13 Å, 2.15 Å and 2.16 Å, respectively (Fig. 6a–c). This is consistent with the order of the metal ionic radii: 0.720 Å (Mg^{2+}) < 0.735 Å (Co^{2+}, high spin) < 0.745 Å (Zn^{2+}). In $Mg_{0.50}Ni_{0.25}Zn_{0.25}O$ (Fig. 6d–f), the distribution ranges of the Mg–O (2.07–2.16 Å) and Zn–O (2.12–2.19 Å) bond lengths are larger than that of $Mg_{0.50}Co_{0.25}Zn_{0.25}O$. The Ni–O bond length distributes around 2.09–2.15 Å, which is ascribed to the smaller radius (0.70 Å) of Ni^{2+}. In $Mg_{0.50}Ni_{0.25}Zn_{0.25}O$, the average bond lengths for Mg–O, Ni–O and Zn–O are 2.12 Å, 2.12 Å and 2.17 Å, respectively. Interestingly, the distributions of Mg–O, Cu–O and Zn–O bond lengths in $Mg_{0.50}Cu_{0.25}Zn_{0.25}O$ (Fig. 6g–i) are much more widespread than that in the other two materials. In particular, the Cu–O bond lengths are distributed across two separate regions, that is, 1.94–2.10 Å and 2.19–2.38 Å, which is attributed to the Jahn–Teller effects of Cu^{2+} ions. The average bond length value of Cu–O is 2.14 Å,

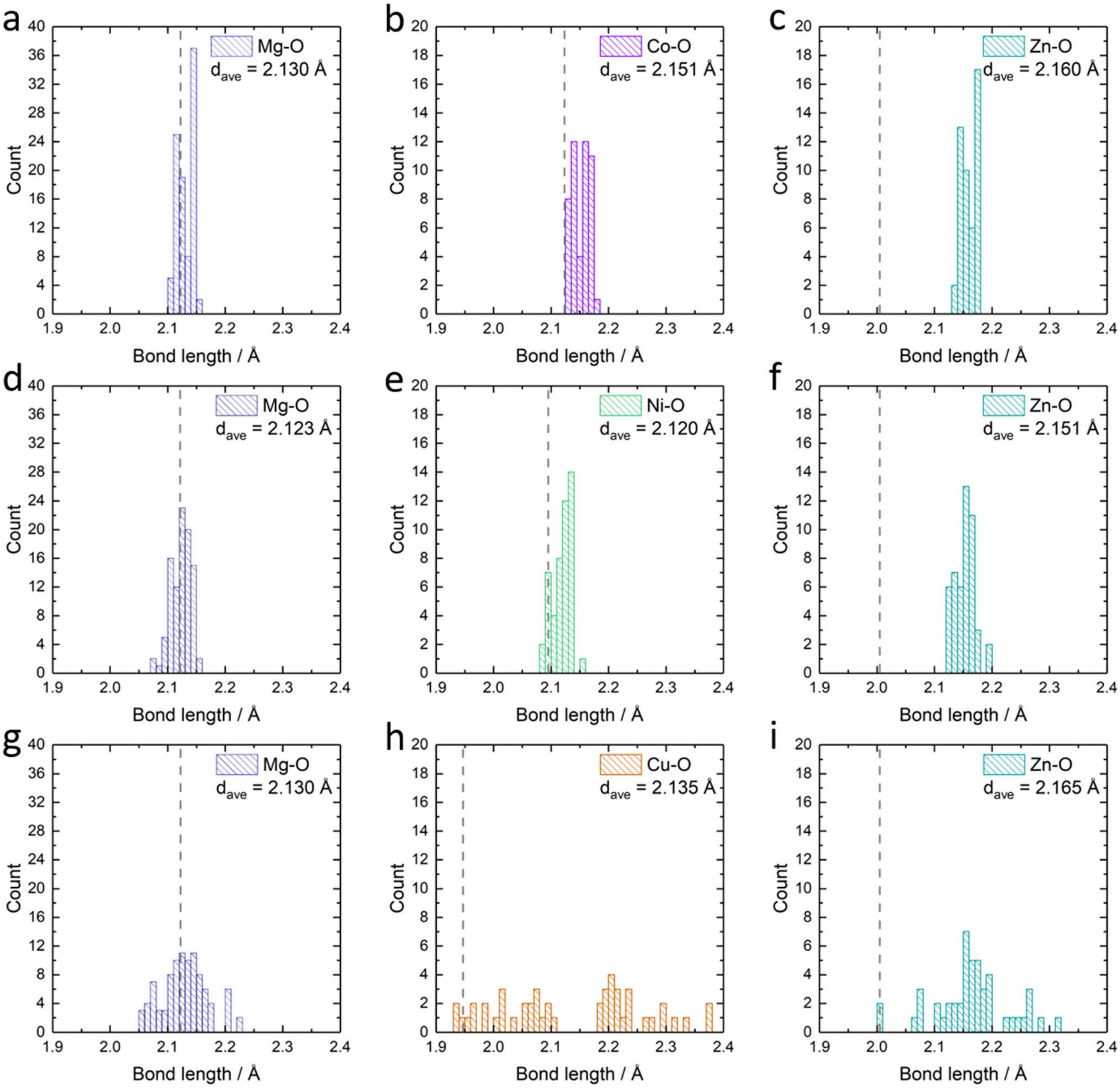

Fig. 6 The statistics of the metal–oxygen bond length in the relaxed structure: the bond-length of (a) Mg–O, (b) Co–O and (c) Zn–O in $Mg_{0.50}Co_{0.25}Zn_{0.25}O$; the bond-length of (d) Mg–O, (e) Ni–O and (f) Zn–O in $Mg_{0.50}Ni_{0.25}Zn_{0.25}O$; the bond-length of (g) Mg–O, (h) Cu–O and (i) Zn–O in $Mg_{0.50}Cu_{0.25}Zn_{0.25}O$. d_{ave} stands for the average metal–oxygen bond length in each panel. The dashed lines indicate the calculated metal–oxygen bond length for metal monoxides: rock-salt MgO in (a), (d) and (g), rock-salt CoO in (b); rock-salt NiO in (e), tenorite CuO in (h), wurtzite ZnO in (c), (f) and (i).

which is smaller than that of Co–O but larger than that of Ni–O. Zn also has a more random Zn–O bond length distribution (2.01–2.31 Å, average bond of 2.17 Å) in $Mg_{0.50}Cu_{0.25}Zn_{0.25}O$. The larger average Zn–O and Cu–O bond lengths in $Mg_{0.50}Cu_{0.25}Zn_{0.25}O$ may partially result from the large distribution range of Cu–O/Zn–O bonds. The bond lengths for Mg–O are in the range of 2.05–2.22 Å with an average of 2.12 Å. Thus, Cu substitution causes a more random metal–oxygen bond length distribution, potentially improving space flexibility for Zn accommodation. However, this flexible space does not exist in $Mg_{0.50}Co_{0.25}Zn_{0.25}O$ and $Mg_{0.50}Ni_{0.25}Zn_{0.25}O$, thus leading to a low Zn stabilization in the rock-salt oxide.

Inferring from the XRD, EXAFS and calculation results, creating a structure with long-range order and short-range disorder is crucial in stabilizing Zn^{2+} ions in the rock-salt oxide. From the perspective of the coordination environment, a properly flexible spatial environment facilitates the Zn stabilization in the rock-salt oxide. When considering the orbitals, such flexible spatial environment is caused by the splitting of e_g orbitals due to the Jahn–Teller distortion. Therefore, in our cases, the short-range disorder and flexible spatial environment produce more remarkable results than increasing configurational entropy by employing the isostructural rock-salt CoO and NiO to stabilize Zn.

3.5 Stability of $Mg_{0.50}TM_{0.25}Zn_{0.25}O$ in alkaline solutions

The stability of $Mg_{0.50}TM_{0.25}Zn_{0.25}O$ (TM = Co, Ni and Zn) in alkaline solutions was evaluated by soaking them in 2 M KOH at room temperature for four weeks under constant stirring. The high-entropy oxide $Mg_{0.2}Co_{0.2}Ni_{0.2}Cu_{0.2}Zn_{0.2}O$ was treated by the same method as a control sample. According to the XRD patterns of these soaked oxides as shown in Fig. 7a, no obvious impurity is observed for soaked $Mg_{0.50}Ni_{0.25}Zn_{0.25}O$ and $Mg_{0.2}Co_{0.2}Ni_{0.2}Cu_{0.2}Zn_{0.2}O$. However, the metal hydroxide ($Mg(OH)_2$/$Co(OH)_2$) phases are observed for soaked $Mg_{0.50}Co_{0.25}Zn_{0.25}O$; and $Mg(OH)_2$ and CuO phases are observed for soaked $Mg_{0.50}Cu_{0.25}Zn_{0.25}O$. Fig. 7b–e demonstrate the atomic ratios of these oxides before and after soaking in KOH (Tables S3–S10†). For soaked $Mg_{0.2}Co_{0.2}Ni_{0.2}Cu_{0.2}Zn_{0.2}O$ and $Mg_{0.50}Ni_{0.25}Zn_{0.25}O$, no obvious change is observed compared to their raw counterparts. For soaked $Mg_{0.50}Co_{0.25}Zn_{0.25}O$, the Zn atomic ratio decreases from 25.7 to 7.5, indicating that the Zn is preferentially leached from $Mg_{0.50}Co_{0.25}Zn_{0.25}O$. Accordingly, this leads to the increase of the atomic ratios of Mg and Co. For soaked $Mg_{0.50}Cu_{0.25}Zn_{0.25}O$, the atomic ratios of Zn and Cu decrease from 23.7 to 9.62 and 23.5 to 19.6, and accordingly, the Mg atomic ratio increases from 52.9 to 70.7, indicating the preferential leaching-out of Zn and Cu. These results suggests that $Mg_{0.50}Ni_{0.25}Zn_{0.25}O$ and $Mg_{0.2}Co_{0.2}Ni_{0.2}Cu_{0.2}Zn_{0.2}O$, which contain Ni, have stronger resistance to alkaline solutions and maintain high structural stability. It should be noted that our results do not imply that metal elements like Co and Ni are completely retained in raw materials. Instead, they indicate that the Zn and Cu are preferentially leached, reducing the structural stability. We did not test the ratio of metal elements in alkaline centrifugates, because we cannot ensure that the powder does not exist in alkaline centrifugates, which could affect the leached element ratios.

From the XPS results (Fig. S23–S26†), one obvious change is the ratio increase at ~531 eV binding energy in the O 1s profile (Fig. 8) for soaked oxides, and this peak also suggests more hydroxides on the surface,[63] which is consistent with the hydroxide appearance from the XRD profile (Fig. 7a). This phenomenon is also expected as more water molecules bound to the surface after soaking, in combination with 531 eV attribution reported by Frankcombe and Liu.[68] Another obvious change is the decrease of the signal-to-noise ratios of the Zn 2p profile for the soaked $Mg_{0.50}Co_{0.25}Zn_{0.25}O$ (Fig. S24†) and $Mg_{0.50}Cu_{0.25}Zn_{0.25}O$ (Fig. S26†), indicating the deduced Zn concentration on the surface. It agrees with the atomic ratio shown in Fig. 7c and e. In addition, the signal-to-noise ratio of the Cu $2p_{3/2}$ profile for the soaked $Mg_{0.2}Co_{0.2}Ni_{0.2}Cu_{0.2}Zn_{0.2}O$ (Fig. S23†) also decreases, suggesting a decreased Cu ratio on the surface. The SEM images of soaked oxides are provided in

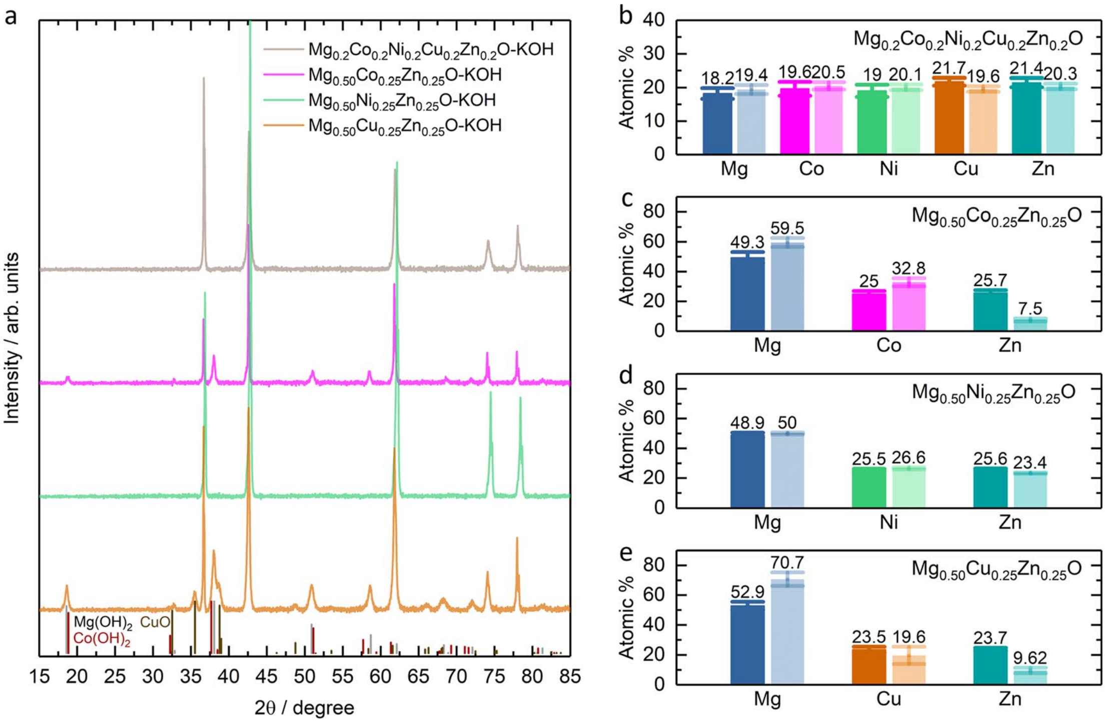

Fig. 7 (a) XRD patterns of $Mg_{0.2}Co_{0.2}Ni_{0.2}Cu_{0.2}Zn_{0.2}O$ and $Mg_{0.50}TM_{0.25}Zn_{0.25}O$ (TM = Co, Ni, Cu) after soaking in 2 M KOH for four weeks, denoted as $Mg_{0.2}Co_{0.2}Ni_{0.2}Cu_{0.2}Zn_{0.2}O$–KOH and $Mg_{0.50}TM_{0.25}Zn_{0.25}O$–KOH. XRD standard peak: $Mg(OH)_2$ refers to PDF 00-007-0239; $Co(OH)_2$ refers to PDF 00-045-0031; CuO refers to PDF 00-045-0937. Atomic percentage of (b) $Mg_{0.2}Co_{0.2}Ni_{0.2}Cu_{0.2}Zn_{0.2}O$ and (c, d and e) $Mg_{0.50}TM_{0.25}Zn_{0.25}O$ before and after soaking in 2 M KOH for four weeks. The bars in dark color are for the raw oxides while the light ones for the soaked samples.

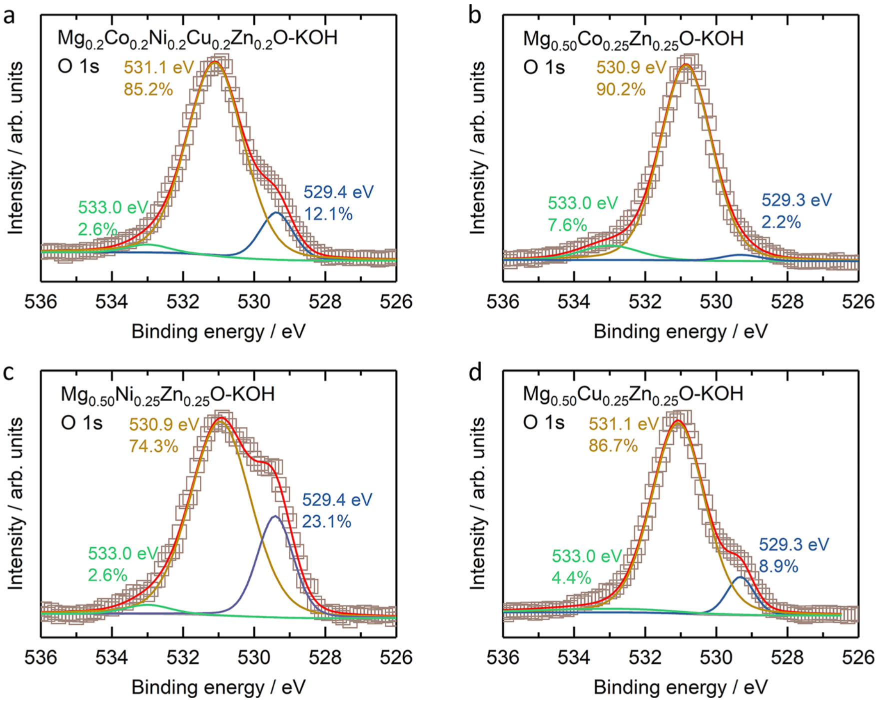

Fig. 8 The O 1s XPS results of (a) $Mg_{0.2}Co_{0.2}Ni_{0.2}Cu_{0.2}Zn_{0.2}O$, (b) $Mg_{0.50}Co_{0.25}Zn_{0.25}O$, (c) $Mg_{0.50}Ni_{0.25}Zn_{0.25}O$, and (d) $Mg_{0.50}Cu_{0.25}Zn_{0.25}O$.

Fig. S27.† The optical photographs of $Mg_{0.50}TM_{0.25}Zn_{0.25}O$ (TM = Co, Ni, Cu) and $Mg_{0.2}Co_{0.2}Ni_{0.2}Cu_{0.2}Zn_{0.2}O$ before and after soaking in 2 M KOH for 4 weeks are also provided in Fig. S28.†

4. Conclusions

In summary, we investigated the roles of Co, Ni and Cu in stabilizing Zn in MgO-based rock-salt oxides. Experimental results demonstrate that incorporation of Co, Ni and Cu increases ZnO solubility in the rock-salt MgO–ZnO system, in which Cu contributes the most to stabilizing Zn despite the absence of rock-salt CuO in nature. Simulation results show that the incorporation of Cu with the Jahn–Teller effect causes a relatively lower formation energy of Zn substitution for Mg and creates a wide metal–oxygen bond length distribution and a flexible space for Zn accommodation, which do not occur in the Co- and Ni-incorporated MgO–ZnO. More importantly, medium-entropy $Mg_{0.50}Cu_{0.25}Zn_{0.25}O$ can also stabilize 25 at% Cu and 25 at% Zn simultaneously like high-entropy $Mg_{0.2}Co_{0.2}Ni_{0.2}Cu_{0.2}Zn_{0.2}O$. The Ni substitution is found effective to improve the structural stability in alkaline media. This work serves as a guide to enable metal stabilization in HEOs by means of short-range disorder and a flexible space environment for rational composition design, and to enable structural stability in alkaline media by metal element selection for future applications in the energy field.

Data availability

The data supporting this article have been included as part of the ESI.†

Author contributions

S. S., J. Z., and S. X. contributed equally to this work. S. S. and Z. W. S. conceived the original concept and initiated the project. S. S. wrote the manuscript. J. Z., S. X., S. W. and Z. W. S. revised it. S. S. synthesized the materials and performed the characterization with assistance from S. X. (XANES and EXAFS), H. R. T. (TEM), F. W. (XRD), D. H. L. S. (XPS), W. Y. L. (XPS) and Y. R. (XPS). S. X. did the EXAFS fitting. J. Z. carried out the theoretical calculation and results analysis. S. W. supervised the simulation work.

Conflicts of interest

There are no conflicts of interest to declare.

Acknowledgements

This work was supported by the Agency for Science, Technology and Research (Central Research Fund Award). We acknowledge the National Supercomputing Centre Singapore for providing the computing resource.

References

1 A. Sarkar, B. Breitung and H. Hahn, *Scr. Mater.*, 2020, **187**, 43–48.
2 C. M. Rost, E. Sachet, T. Borman, A. Moballegh, E. C. Dickey, D. Hou, J. L. Jones, S. Curtarolo and J. P. Maria, *Nat. Commun.*, 2015, **6**, 8485.

3 A. Sarkar, Q. Wang, A. Schiele, M. R. Chellali, S. S. Bhattacharya, D. Wang, T. Brezesinski, H. Hahn, L. Velasco and B. Breitung, *Adv. Mater.*, 2019, **31**, e1806236.

4 A. Amiri and R. Shahbazian-Yassar, *J. Mater. Chem. A*, 2021, **9**, 782–823.

5 C. Oses, C. Toher and S. Curtarolo, *Nat. Rev. Mater.*, 2020, **5**, 295–309.

6 S. Schweidler, M. Botros, F. Strauss, Q. Wang, Y. Ma, L. Velasco, G. C. Marques, A. Sarkar, C. Kübel, H. Hahn, J. Aghassi-Hagmann, T. Brezesinski and B. Breitung, *Nat. Rev. Mater.*, 2024, **9**, 266–281.

7 B. Ouyang and Y. Zeng, *Nat. Commun.*, 2024, **15**, 973.

8 M. V. Kante, M. L. Weber, S. Ni, I. C. G. van den Bosch, E. van der Minne, L. Heymann, L. J. Falling, N. Gauquelin, M. Tsvetanova, D. M. Cunha, G. Koster, F. Gunkel, S. Nemsak, H. Hahn, L. Velasco Estrada and C. Baeumer, *ACS Nano*, 2023, **17**, 5329–5339.

9 T. X. Nguyen, Y. C. Liao, C. C. Lin, Y. H. Su and J. M. Ting, *Adv. Funct. Mater.*, 2021, **31**, 2101632.

10 R. R. Katzbaer, F. M. Dos Santos Vieira, I. Dabo, Z. Mao and R. E. Schaak, *J. Am. Chem. Soc.*, 2023, **145**, 6753–6761.

11 J. Wang, S. Sun, S. Xi, Y. Sun, S. J. H. Ong, Z. W. Seh and Z. J. Xu, *J. Phys. Chem. C*, 2024, **128**, 4978–4987.

12 C. Liu, J. Bi, L. Xie, X. Gao and J. Rong, *J. Energy Storage*, 2023, **71**, 108211.

13 S. Sun, C. Dai, P. Zhao, S. Xi, Y. Ren, H. R. Tan, P. C. Lim, M. Lin, C. Diao, D. Zhang, C. Wu, A. Yu, J. C. J. Koh, W. Y. Lieu, D. H. L. Seng, L. Sun, Y. Li, T. L. Tan, J. Zhang, Z. J. Xu and Z. W. Seh, *Nat. Commun.*, 2024, **15**, 260.

14 A. Sarkar, L. Velasco, D. Wang, Q. Wang, G. Talasila, L. d. Biasi, C. Kübel, T. Brezesinski, S. S. Bhattacharya, H. Hahn and B. Breitung, *Nat. Commun.*, 2018, **9**, 3400.

15 Q. Wang, A. Sarkar, Z. Li, Y. Lu, L. Velasco, S. S. Bhattacharya, T. Brezesinski, H. Hahn and B. Breitung, *Electrochem. Commun.*, 2019, **100**, 121–125.

16 Z. Lun, B. Ouyang, D. H. Kwon, Y. Ha, E. E. Foley, T. Y. Huang, Z. Cai, H. Kim, M. Balasubramanian, Y. Sun, J. Huang, Y. Tian, H. Kim, B. D. McCloskey, W. Yang, R. J. Clement, H. Ji and G. Ceder, *Nat. Mater.*, 2021, **20**, 214–221.

17 F. Liu, M. Yu, X. Chen, J. Li, H. Liu and F. Cheng, *Chin. J. Catal.*, 2022, **43**, 122–129.

18 N. Qiu, H. Chen, Z. Yang, S. Sun, Y. Wang and Y. Cui, *J. Alloys Compd.*, 2019, **777**, 767–774.

19 P. Ghigna, L. Airoldi, M. Fracchia, D. Callegari, U. Anselmi-Tamburini, P. D'Angelo, N. Pianta, R. Ruffo, G. Cibin, D. O. de Souza and E. Quartarone, *ACS Appl. Mater. Interfaces*, 2020, **12**, 50344–50354.

20 K. Wang, W. Hua, X. Huang, D. Stenzel, J. Wang, Z. Ding, Y. Cui, Q. Wang, H. Ehrenberg, B. Breitung, C. Kubel and X. Mu, *Nat. Commun.*, 2023, **14**, 1487.

21 E. Lokcu, C. Toparli and M. Anik, *ACS Appl. Mater. Interfaces*, 2020, **12**, 23860–23866.

22 X. Liu, Y. Xing, K. Xu, H. Zhang, M. Gong, Q. Jia, S. Zhang and W. Lei, *Small*, 2022, **18**, e2200524.

23 M. Fracchia, M. Coduri, M. Manzoli, P. Ghigna and U. A. Tamburini, *Nat. Commun.*, 2022, **13**, 2977.

24 S. S. Aamlid, M. Oudah, J. Rottler and A. M. Hallas, *J. Am. Chem. Soc.*, 2023, **145**, 5991–6006.

25 M. Brahlek, M. Gazda, V. Keppens, A. R. Mazza, S. J. McCormack, A. Mielewczyk-Gryń, B. Musico, K. Page, C. M. Rost, S. B. Sinnott, C. Toher, T. Z. Ward and A. Yamamoto, *APL Mater.*, 2022, **10**, 110902.

26 K. Chen, J. Ma, H. Wang, C. Li and L. An, *Ceram. Int.*, 2021, **47**, 9979–9983.

27 J. E. Jaffe, R. Pandey and A. B. Kunz, *Phys. Rev. B: Condens. Matter Mater. Phys.*, 1991, **43**, 14030–14034.

28 S. R. Kelly, X. Shi, S. Back, L. Vallez, S. Y. Park, S. Siahrostami, X. Zheng and J. K. Nørskov, *ACS Catal.*, 2019, **9**, 4593–4599.

29 J. Pfrommer, M. Lublow, A. Azarpira, C. Gobel, M. Lucke, A. Steigert, M. Pogrzeba, P. W. Menezes, A. Fischer, T. Schedel-Niedrig and M. Driess, *Angew Chem., Int. Ed. Engl.*, 2014, **53**, 5183–5187.

30 M. R. Shakil, A. M. El-Sawy, H. Tasnim, A. G. Meguerdichian, J. Jin, J. P. Dubrosky and S. L. Suib, *Inorg. Chem.*, 2018, **57**, 9977–9987.

31 R. Subhash Kanase, G. Mulualem Zewdie, M. Arunachalam, J. Badiger, S. Abdelfattah Sayed, K.-S. Ahn, J.-S. Ha, U. Sim, H. Shin and S. Hyung Kang, *J. Energy Chem.*, 2024, **88**, 71–81.

32 X. Jiang, F. Cai, D. Gao, J. Dong, S. Miao, G. Wang and X. Bao, *Electrochem. Commun.*, 2016, **68**, 67–70.

33 G. Zhang, S. Hou, H. Zhang, W. Zeng, F. Yan, C. C. Li and H. Duan, *Adv. Mater.*, 2015, **27**, 2400–2405.

34 W. Chang, J.-W. Choi, J.-C. Im and J. K. Lee, *J. Power Sources*, 2010, **195**, 320–326.

35 A. J. Laghari, U. Aftab, A. Tahira, A. A. Shah, A. Gradone, M. Y. Solangi, A. H. Samo, M. kumar, M. I. Abro, M. w. Akhtar, R. Mazzaro, V. Morandi, A. M. Alotaibi, A. Nafady, A. Infantes-Molina and Z. H. Ibupoto, *Int. J. Hydrogen Energy*, 2023, **48**, 12672–12682.

36 X. He, J. Tan, J. Wei, F. Yin, B. Chen, X. Liang and G. Li, *Appl. Surf. Sci.*, 2020, **508**, 144758.

37 Y.-z. Su, Q.-z. Xu, Q.-s. Zhong, C.-j. Zhang, S.-t. Shi and C.-w. Xu, *Mater. Res. Bull.*, 2015, **64**, 301–305.

38 C. Xu, P. K. Shen, X. Ji, R. Zeng and Y. Liu, *Electrochem. Commun.*, 2005, **7**, 1305–1308.

39 H. Sclar, O. Haik, T. Menachem, J. Grinblat, N. Leifer, A. Meitav, S. Luski and D. Aurbach, *J. Electrochem. Soc.*, 2012, **159**, A228–A237.

40 Y. Wang, Y.-F. Zhang, H.-R. Liu, S.-J. Yu and Q.-Z. Qin, *Electrochim. Acta*, 2003, **48**, 4253–4259.

41 B. Xu, H. Shen, J. Ge and Q. Tang, *Appl. Surf. Sci.*, 2021, **546**, 148814.

42 J. S. Gnanaraj, V. G. Pol, A. Gedanken and D. Aurbach, *Electrochem. Commun.*, 2003, **5**, 940–945.

43 A. van de Walle, P. Tiwary, M. de Jong, D. L. Olmsted, M. Asta, A. Dick, D. Shin, Y. Wang, L. Q. Chen and Z. K. Liu, *Calphad*, 2013, **42**, 13–18.

44 G. Kresse and J. Hafner, *Phys. Rev. B: Condens. Matter Mater. Phys.*, 1993, **47**, 558–561.

45 G. Kresse and J. Hafner, *Phys. Rev. B: Condens. Matter Mater. Phys.*, 1994, **49**, 14251–14269.

46 G. Kresse and D. Joubert, *Phys. Rev. B: Condens. Matter Mater. Phys.*, 1999, **59**, 1758–1775.

47 J. Hubbard, *Proc. R. Soc. London, Ser. A*, 1963, **276**, 238–257.

48 S. L. Dudarev, G. A. Botton, S. Y. Savrasov, C. J. Humphreys and A. P. Sutton, *Phys. Rev. B: Condens. Matter Mater. Phys.*, 1998, **57**, 1505–1509.

49 G. C. Moore, M. K. Horton, E. Linscott, A. M. Ganose, M. Siron, D. D. O'Regan and K. A. Persson, *Phys. Rev. Mater.*, 2024, **8**, 014409.

50 R. D. Shannon and C. T. Prewitt, *Acta Crystallogr.*, 1969, **B25**, 925–946.

51 D. Berardan, A. K. Meena, S. Franger, C. Herrero and N. Dragoe, *J. Alloys Compd.*, 2017, **704**, 693–700.

52 M. A. Peck and M. A. Langell, *Chem. Mater.*, 2012, **24**, 4483–4490.

53 B. K. Teo, Data analysis in practice, in *EXAFS: Basic Principles and Data Analysis*, Springer, Berlin, Heidelberg, 1986, ch. 6, p. 124.

54 J. Sushil, A. Kumar, A. Gautam and M. I. Ahmad, *Mater. Chem. Phys.*, 2021, **259**, 124014.

55 O. J. Marques, C. Chen, E. V. Timofeeva and C. U. Segre, *J. Power Sources*, 2023, **564**, 232852.

56 C. M. Rost, Z. Rak, D. W. Brenner and J. P. Maria, *J. Am. Ceram. Soc.*, 2017, **100**, 2732–2738.

57 A. Rodrigues, M. d. C. M. Alves and J. Morais, *Mater. Des.*, 2018, **142**, 240–246.

58 A. N. Baranov, P. S. Sokolov, V. A. Tafeenko, C. Lathe, Y. V. Zubavichus, A. A. Veligzhanin, M. V. Chukichev and V. L. Solozhenko, *Chem. Mater.*, 2013, **25**, 1775–1782.

59 M. C. Biesinger, B. P. Payne, A. P. Grosvenor, L. W. M. Lau, A. R. Gerson and R. S. C. Smart, *Appl. Surf. Sci.*, 2011, **257**, 2717–2730.

60 J. Yang, H. Liu, W. N. Martens and R. L. Frost, *J. Phys. Chem. C*, 2010, **114**, 111–119.

61 Y. Lykhach, S. Piccinin, T. Skala, M. Bertram, N. Tsud, O. Brummel, M. Farnesi Camellone, K. Beranova, A. Neitzel, S. Fabris, K. C. Prince, V. Matolin and J. Libuda, *J. Phys. Chem. Lett.*, 2019, **10**, 6129–6136.

62 K. Tanwar, D. S. Gyan, S. Bhattacharya, S. Vitta, A. Dwivedi and T. Maiti, *Phys. Rev. B*, 2019, **99**, 174105.

63 N. S. McIntyre and M. G. Cook, *Anal. Chem.*, 1975, **47**, 2208–2213.

64 K. J. Gaskell, A. Starace and M. A. Langell, *J. Phys. Chem. C*, 2007, **111**, 13912–13921.

65 S. Hüfner, Charge-excitation final states: satellites in *Photoelectron Spectroscopy Principles and Applications*, Springer, Berlin, Heidelberg, 2003, ch. 3, pp. 29–130.

66 S. Altieri, L. H. Tjeng, A. Tanaka and G. A. Sawatzky, *Phys. Rev. B: Condens. Matter Mater. Phys.*, 2000, **61**, 13403–13409.

67 J. C. C. Fan and J. B. Goodenough, *J. Appl. Phys.*, 1977, **48**, 3524–3531.

68 T. J. Frankcombe and Y. Liu, *Chem. Mater.*, 2023, **35**, 5468–5474.